PHOTONICS Research

Revealing of the ultrafast third-order nonlinear optical response and enabled photonic application in two-dimensional tin sulfide

Zhongjian Xie,[1,†] Feng Zhang,[1,†] Zhiming Liang,[1,†] Taojian Fan,[1] Zhongjun Li,[2] Xiantao Jiang,[1,3,5] ⓘ
Hong Chen,[4,6] Jianqing Li,[2] ⓘ and Han Zhang[1,*] ⓘ

[1]Shenzhen Engineering Laboratory of Phosphorene and Optoelectronics, Key Laboratory of Optoelectronic Devices and Systems of Ministry of Education and Guangdong Province, College of Optoelectronic Engineering, Shenzhen University, Shenzhen 518060, China
[2]Faculty of Information Technology, Macau University of Science and Technology, Macao, China
[3]College of Chemistry and Environmental Engineering, Shenzhen University, Shenzhen 518060, China
[4]School of Materials Science and Energy Engineering, Foshan University, Foshan 528000, China
[5]e-mail: jiangxtemail@sina.com
[6]e-mail: chenhongcs@126.com
*Corresponding author: hzhang@szu.edu.cn

Black phosphorus (BP), a typical mono-elemental and two-dimensional (2D) material, has gathered significant attention owing to its distinct optoelectronic properties and promising applications, despite its main obstacle of long-term stability. Consequently, BP-analog materials with long-term chemical stability show additional potential. In this contribution, tin sulfide (SnS), a novel two-elemental and 2D structural BP-analog monochalcogenide, has been demonstrated to show enhanced stability under ambient conditions. The broadband nonlinear optical properties and carrier dynamics have been systematically investigated via *Z*-scan and transient absorption approaches. The excellent nonlinear absorption coefficient of 50.5×10^{-3} cm/GW, 1 order of magnitude larger than that of BP, endows the promising application of SnS in ultrafast laser generation. Two different decay times of $\tau_1 \sim 873$ fs and $\tau_2 \sim 96.9$ ps allow the alteration between pure *Q* switching and continuous-wave (CW) mode locking in an identical laser resonator. Both mode-locked and *Q*-switched operations have been experimentally demonstrated using an SnS saturable absorber at the telecommunication window. Femtosecond laser pulses with tunable wavelength and high stability are easily obtained, suggesting the promising potential of SnS as an efficient optical modulator for ultrafast photonics. This primary investigation may be considered an important step towards stable and high-performance BP-analog material-based photonic devices. © 2019 Chinese Laser Press

https://doi.org/10.1364/PRJ.7.000494

1. INTRODUCTION

Black phosphorus (BP), a typical 2D material, recently has gained significant attention in the communities of electronics and optoelectronics [1–3]. It features a unique layer-dependent direct bandgap [4], which can be adjusted from ~0.3 eV (bulk) to ~2 eV (monolayer), right filling up the bandgap interval between 0 eV of graphene and large values of transition metal dichalcogenides (TMDCs). The thickness of sensitive direct bandgap is favorable for its optoelectronic applications covering from the near- to mid-infrared spectrum. Recently, a series of investigations revealed that the saturable absorption of BP can span from 0.4 to 2.8 μm, indicating its potential for pulse generation [5]. Lately, BP has also been developed as an optical saturable absorber (SA) for both passively *Q*-switched

and mode-locked fiber lasers at 1.55 μm with excellent performance [6–8].

Despite these favorable properties of BP, a main drawback is its long-term stability [9]. BP is sensitive to water and oxygen under ambient conditions because of the high activity of phosphorus atoms and the fragile atomic binding [10], resulting in compositional changes and consequent degradation of the electronic and optical performance [11–15]. This severely hinders its applications in flexible electronics, photoelectrons, and electrochemical applications.

To address this drawback, several protection methods have been reported, including covalent bonding with aryl diazonium [16] and carbon free radicals [17], introduction of fluorine adatoms [18], intercalation of alkali metal hydrides [19],

metal-ion modification [20], surface coordination of titanium sulfonate ligand [17], and encapsulation by graphene shell [14], hexagonal boron nitride (BN) [11,21], graphene oxide [22], AlO_x [15,23], organic monolayers, etc. [24]. Although the high stability of BP has been reached, those strategies bring either the advanced synthesis of functional groups or post-treatment of prepared BP nanomaterials, which result in the technical complexity for fabricating BP [25].

A demand for highly stable 2D nanomaterials drives researchers to search for other high-quality BP analog materials with enhanced long-term stability. Fortunately, a group of layered group IV monochalcogenides, such as SnSe [26], GeSe [27], GeS [28], and SnS [29] have puckered structures similar to BP. Bulk SnSe has shown great potential in thermoelectric applications [30,31]. Recently, inspired by the unique property of anisotropic structure in phosphorene, 2D monochalcogenides have attracted great research interest [32–35], especially for their thermoelectric properties [31,36]. Furthermore, compared with the single element in phosphorene, these monochalcogenides are composed of two different types of elements and thus possess different electronegativity [37]. These features can lead to more complicated physics phenomena than that of phosphorene. Indeed, some unique properties, such as giant piezoelectricity [38] and multiferroic with coupled ferroelectricity and ferroelasticity [33,34] have been theoretically proposed. At the same time, experimental investigations on 2D monochalcogenides are in progress [26,39]. SnS exhibits strong anisotropic mechanical and optoelectronic features [37,39–44]. The presence of weak van der Waals force between SnS layers shows no dangling bonds, giving a chemically inert surface [45]. As a result, SnS shows chemical stability even in acidic solution [46], a high melting point of 880°C, and a boiling point of 1230°C. In view of the environment, the Sn and S elements are relatively abundant, and they are safe elements [47]. These favorable properties make SnS a potential material for various applications, including photovoltaics [48,49], solid-state batteries [50,51], thermoelectricity [52], humidity sensors [53], supercapacitor electrodes [54], solar hydrogen production [55], etc.

SnS possesses unique dual direct and indirect bandgaps, with the direct bandgap varying from 1.30 to 1.39 eV and the indirect bandgap from 1.07 to 1.25 eV [42]. In another report, the bandgap of SnS can be adjusted from 1.03 to 1.65 eV [56]. Moreover, it possesses large absorption coefficients ($>10^4$ cm^{-1}), spanning the ultraviolet to near-infrared (NIR) regions [29,56]. Its carrier mobility was predicted to be tens of thousands of $cm^2 \cdot V^{-1} \cdot s^{-1}$ [29], which is even faster than that of BP. Owing to the suitable and tunable bandgap and fast carrier mobility of SnS, excellent nonlinear optical properties can be anticipated. However, investigation of such properties and optoelectronic applications in NIR regions is still in its infancy stage.

In this work, the BP-analog SnS was thus investigated as a new type of effective SA. The high stability of as-prepared SnS nanosheets (NSs) was confirmed through systematic characterizations. Nonlinear absorption was characterized at 800 and 1550 nm, respectively, both exhibiting excellent SA properties. High and tunable modulation depth makes it flexible

as a *Q* switcher and mode locker. The carrier dynamics, presented by two time components, namely, electron thermalization within the band (873 fs) and recombination of the carriers (96.9 ps), indicates the promising potential of SnS for mode locking. The ultrafast (656 fs) pulse generation in fiber lasers based on SnS NSs was experimentally demonstrated at 1560 nm with high stability. This primary study opens a new avenue for advanced electrophotonics by using BP-analog 2D nanomaterials, suggesting the great promise of group IV monochalcogenides as the substitutions.

2. RESULTS AND DISCUSSION

A. Fabrication and Characterizations

SnS NSs were prepared with the liquid-phase exfoliation (LPE) method. N-methyl-2-pyrrolidone (NMP) was normally chosen to exfoliate SnS [56]. The solvent of isopropyl alcohol (IPA) was chosen to exfoliate SnS in this work because of its lower boiling point, leading to easy removal. In Fig. 1(a), the transmission electron microscopy (TEM) image shows SnS NSs with a main 2D size of ∼50 nm and a thickness of less than ∼6 nm, as shown by the atomic force microscopy (AFM) image [Fig. 1(b)]. The (210) and (111) planes with interatomic space of 0.32 and 0.30 nm are determined by the observation of high-resolution TEM (HRTEM) [Fig. 1(c)] [57]. Fast Fourier transformation (FFT) of the crystal lattice shows the expected crystallographic lattice reflections [inset of Fig. 1(c)]. The selected-area electron diffraction (SAED) image in Fig. 1(d) suggests that the crystal phase of the SnS NSs remains after the LPE procedure, corresponding to the FFT calculation of the crystal lattice.

The crystal phases of SnS NSs and bulk SnS were compared by employing X-ray diffraction (XRD) and Raman techniques. In Fig. 1(e), both the SnS NSs and bulk SnS exhibited a similar typical XRD pattern. For Raman spectroscopy of bulk SnS, three clear Raman peaks were shown from 100 to 500 cm^{-1}. The B_{3g} mode locates at 161.8 cm^{-1}, and the A_g mode is responsible for the peaks at 185.5 and 219.9 cm^{-1}. The peak at ∼300 cm^{-1} comes from SnS_2 owing to the surface oxidation [57,58]. For SnS NSs, the peaks at 163.7 cm^{-1} (B_{3g}) and 190.9 cm^{-1} (A_g) indicate a Raman shift compared with the bulk SnS, especially for the A_g mode (from 185.5 to 190.9 cm^{-1}). It can be concluded that the A_g mode shows the more sensitive layer-dependent behavior in the two vibrational modes because it is along the armchair direction. The energy-dispersive X-ray spectroscopy (EDX) mapping in scanning transmission electron microscopy (STEM) mode presented the composition of Sn and S elements in SnS NSs [Fig. 1(g)]. All measurements determine the composition and crystal phase of the exfoliated SnS NSs.

Concerning the optical applications, the as-exfoliated SnS NSs must possess sufficiently high stability. The stability of SnS NSs was systematically characterized by absorbance spectrum, XRD pattern, Raman spectroscopy, and X-ray photoelectron spectroscopy (XPS). The absorbance of SnS NSs remains stable in 30 days, as shown in Fig. 2(a). Both the XRD pattern and Raman spectrum in 30 days present similar peaks [Figs. 2(b) and 2(c)]. For the XPS characterization [Fig. 2(d)], Sn 3d 5/2 and 3d 3/2 orbitals are responsible for the strong
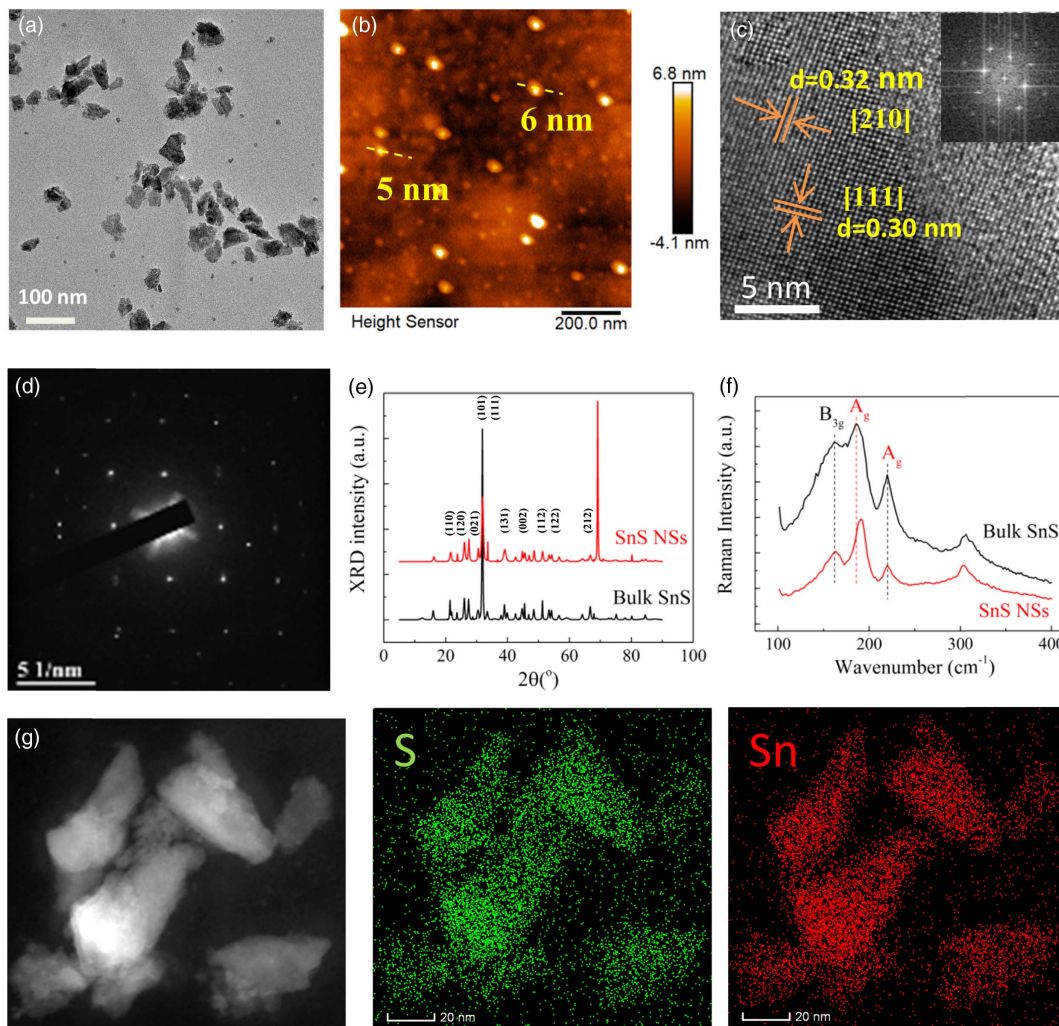
Fig. 1. Typical characterizations of the SnS NSs. (a) TEM image; (b) AFM image; (c) crystal lattice shown by HRTEM image and corresponding FFT; (d) crystalline features shown by SAED; (e) XRD pattern; (f) Raman spectra of bulk SnS and exfoliated SnS NSs; (g) element distribution mapping via STEM.

peaks at 485.6 and 494.1 eV, respectively. After 30 days, there was no obvious energy shift. All these characterizations indicate the high stability of SnS NSs in ambient conditions.

B. Saturable Absorption Properties of SnS NSs

The steady-state optical response is determined by ultraviolet-visible-near-infrared (UV-vis-NIR) absorption from 350 to 1680 nm, which is measured in IPA solution when the influence of solution has been removed (Fig. 3). From 350 to ∼800 nm, the absorbance decreased quasi-linearly, and the absorbance remained almost stable from ∼800 to ∼1100 nm. It was interesting to find that there were two absorbance peaks centralized at 1180 and 1480 nm, corresponding to the bandgap of 1.05 and 0.84 eV [Fig. 3(a)]. According to the Tauc plot [Fig. 3(b)], the bandgap of SnS NSs was fitted to be 1.2 eV, similar to the previous report [56]. Therefore, the two above-mentioned absorbance peaks belonged to the subbandgap absorption, which may be caused by crystal defect. These two absorbance peaks strongly suggested that the SnS NSs might be a promising optical material in the telecommunication band.
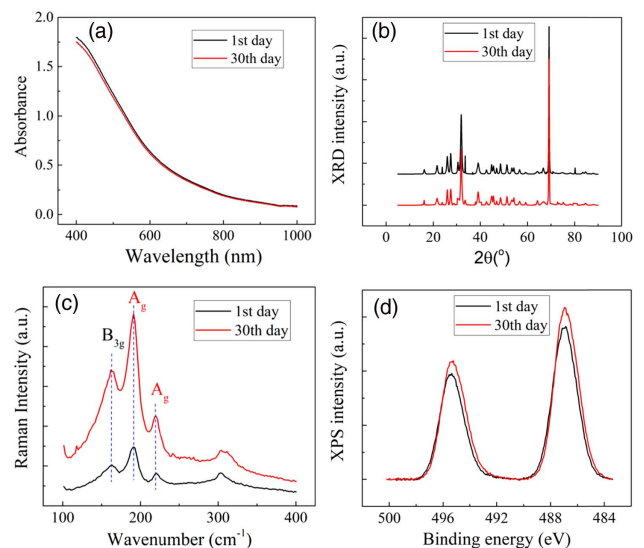

Fig. 2. Stability of SnS NSs in ambient conditions characterized by (a) absorbance, (b) XRD, (c) Raman, and (d) XPS spectra, respectively.
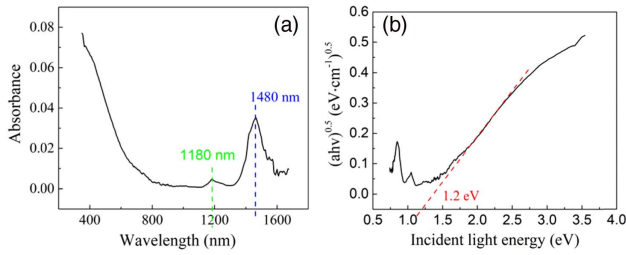
Fig. 3. (a) Linear optical absorption spectrum of SnS NSs from the UV to NIR region in IPA solution. The baseline of IPA has been removed. (b) Corresponding Tauc plot of the linear optical absorption spectrum.
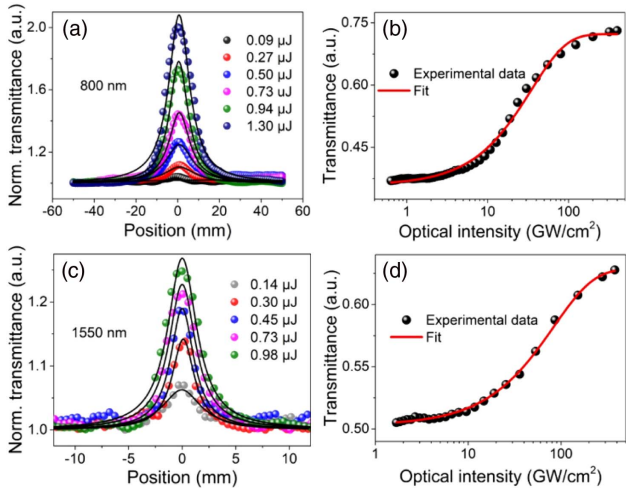

Fig. 4. Normalized transmittance versus z axis at different pulse energies [(a) 800 nm, (c) 1550 nm], and the corresponding intensity-dependent transmittance fitted via a two-level energy model [(b) 800 nm, (d) 1550 nm].

Broadband nonlinear optical absorption of SnS NSs is then characterized by the well-developed Z-scan technique [5,59]. Under high optical intensity, the total nonlinear absorption could be attributed to various nonlinear absorption mechanisms, including ground state bleaching (GSB), excited state absorption (ESA), two-photon absorption (TPA), and multiphoton absorption (MPA), etc. To characterize nonlinear absorption of few-layer SnS NSs, the transmittance versus the z axis was recorded. Strong saturable absorption was observed at both 800 and 1550 nm (Fig. 4). Materials with such significant properties can be used as an efficient optical modulator for Q switching or mode-locking operations.

The absorption coefficient of the SnS NSs can be written as

$$\alpha = \alpha_0 + \alpha_{NL}, \tag{1}$$

where α_0 is the linear absorption part, $\alpha_{NL} = \beta I$ is the nonlinear part (β is the nonlinear absorption coefficient and I is the incident optical intensity). The linear absorption coefficient is independent of the optical intensity, which can be obtained at low intensity using the equation $\alpha_0 = \frac{\ln(LT)}{L}$, where LT is the linear transmittance (shown in Table 1), and L is the length of light path traversing SnS dispersion. α_{NL} is strongly dependent on intensity and β can be deduced by fitting normalized transmittance $T_{norm(z)}$ versus z axis using the equation [60]

$$T_{norm(z)} = \ln[1 + q_0(z)]/q_0(z), \tag{2}$$

where $q_0(z) = \beta I_0 L_{eff}(1 + z^2/z_0^2)$, I_0 is the on-axis optical intensity, $L_{eff} = [1 - \exp(-\alpha_0 L)]/\alpha_0$ is the effective propagation length, and z_0 is the Rayleigh length. Normalized transmittance versus the pulse energy and the corresponding fitting curves at 800 nm are shown in Fig. 4(a); β is fitted to be $-(50.5 \pm 3.4) \times 10^{-3}$ cm/GW at the maximum pulse energy of 1.30 μJ. Considering the contribution of third-order nonlinear susceptibility to saturable absorption, the imaginary part of third-order susceptibility (Im $\chi^{(3)}$) has a positive correlation with β [61], Im $\chi^{(3)} = \frac{2\varepsilon_0 c^2 n_0^2}{3\omega} \beta$, where c is the light speed in vacuum, ε_0 is the vacuum permittivity, n_0 is the linear refractive index ($n_0 \approx 1.373$ for IPA solvent [62]), and ω is the angular frequency of the light. Im $\chi^{(3)}$ is calculated to be 4.25×10^{-21} m^2/V^2 at the pulse energy of 1.30 μJ. For 1550 nm, the Z-scan results and fitting curves are shown in Fig. 4(c), and the corresponding β and Im $\chi^{(3)}$ are summarized in Table 1.

To further characterize the saturable absorption properties of SnS NSs, the relation between the transmittance and optical intensity [Fig. 4(b)] can be obtained from the Z-scan results using the equation

$$I = I_0/(1 + z^2/z_0^2). \tag{3}$$

The transmittance versus the optical intensity can be fitted by a simple saturable absorption model [63]

$$T = 1 - \Delta T \times \exp(-I/I_s) - T_{ns}, \tag{4}$$

where ΔT, I_s, T_{ns} are modulation depth, saturation optical intensity, and nonsaturable loss, respectively. As a BP-analog material, parameters of the SnS are compared with the widely investigated BP [5]. For an SA, higher ΔT means the stronger ability to modulate the intensity of the light. A higher value of ΔT was calculated to be 36.4% for SnS NSs, compared to other single-elemental 2D materials, including

Table 1. Value of LT, ΔT, T_{ns}, I_s, β, Im $\chi^{(3)}$ for SnS@800 nm, 1550 nm and BP@800 nm under the pulse energy of 1.3 μJ/pulse and 1.0 μJ/pulse

	LT (%)	ΔT (%)	T_{ns} (%)	I_s (GW/cm^2)	β (10^{-3} cm/GW)	Im $\chi^{(3)}$ (10^{-21} m^2/V^2)
SnS@800nm	35.9	36.4	27.7	34.8 ± 1.2	$-(50.5 \pm 3.4)$	4.25 ± 0.28
SnS@1550 nm	50.4	12.5	37.1	83.5 ± 2.5	$-(14.1 \pm 0.3)$	2.30 ± 0.05
BP@800 nm	85.6	12.4	1.9	334.6 ± 43	$-(6.17 \pm 0.19)$	—

bismuthene (2.03%) [64], antimonene (6.4%) [65], newly found 2D Se (2.13%) [66], as well as BP (12.4%). Additionally, the value of I_s is 1 order smaller than that of the BP, which can help to reduce the threshold of the SA-based mode-locked or Q-switched lasers. Moreover, the nonlinear coefficient β of SnS NSs was found to be larger than that of BP, illustrating the stronger interaction between light and SnS NSs (Table 1). These excellent saturable absorption properties at the communication band mean SnS can be a quite promising candidate as an optical modulator.

C. Characterization of the Relaxation Time

The relaxation time of the charge carriers is a fundamental parameter for semiconductors and significantly affects the performance of that based optoelectronic devices, such as photodetectors, solar cells, and pulsed lasers. The photo-induced carrier dynamics of SnS NSs was investigated with the assistance of a femtosecond-resolved transient absorption (TA) spectrometer. A nondegenerate setup with broad NIR probe band (1000–1500 nm) was employed. Pumped at 400 nm, clearly photon-induced absorption of SnS NSs was observed within the probe band. Figures 5(a) and 5(b) show the TA spectra at the delay line of 0-5.0 ps, which suggests the cooling speed is fast at the beginning, and then becomes slow when the delay line surpasses 5.0 ps. By global time analysis [67], one principal spectrum and kinetic of the charge carrier are figured out, which can well recall the relaxation dynamics [Fig. 5(c)]. ΔA is the absorption difference for the probe light with/without the pump light. The electrons are excited to high conduction band in the first 400 fs through the Franck–Condon transition, leaving over the holes in the valence band. The cooling dynamics for SnS NSs can be divided into two processes. Initially, the electrons undergo thermal equilibrium in the conduction band within 873 fs, and then the hot electrons cool down to the valence band and recombine with the holes at 96.9 ps. The probe wavelength-dependent ΔA can be fitted using a dual-exponential decay model

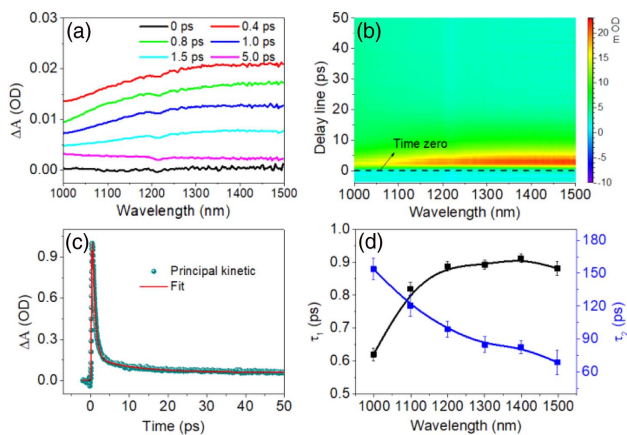$$\Delta A = A_1 \exp(-t/\tau_1) + A_2 \exp(-t/\tau_2), \qquad (5)$$

Fig. 5. (a) TA spectra of the SnS sample in the time scale of 0–5.0 ps; (b) 2D mapping of the TA spectrum from 1000 to 1500 nm; (c) principal dynamic figured out by singular value decomposition; (d) decay time τ_1 and τ_2 versus the probe wavelength.

where τ_1 is short decay time and τ_2 is long decay time. In Fig. 5(d), it was observed the short decay time τ_1 increased from 620.2 ± 19.8 to 912.1 ± 12.58 fs as the probe wavelength increased from 1000 to 1500 nm, while the long decay time τ_2 decreased from 153.8 ± 9.5 to 68.9 ± 11.0 ps. The trend of τ_1 and τ_2 means intraband scattering dynamic constant (τ_2) has a negative correlation with probe wavelength and the interband scattering constant (τ_1) has a positive correlation with the wavelength.

Mode locking based on slow SA, that is to say, the pulse width can be smaller than the recovery time, has been proved to be an effective passive technique to generate ultrafast lasers other than the fast SA-like Kerr mode locking for the highly restrictive cavity design. Semiconductor saturable absorber mirrors (SESAMs) [68], and the SA based on recently developed 2D materials, like graphene, TMDs, and BP, enrich the diversity of the slow SA [5,69–71]. For an SESAM, response time associated with the photoinduced electrons and holes relaxation dynamics significantly dominates the performance of the optical devices. It is believed that the short time constant (τ_1) is the intrinsic character of one kind of material, and the order of hundreds of femtoseconds for SnS materials is suitable for starting the mode locking [72]. While the long time constant (τ_2), usually in the time scale from several picoseconds to hundreds of picoseconds, plays an important role in sustaining the mode locking, SnS semiconductor possesses relatively long τ_1 than graphene and BP [5,69]. Therefore, both mode-locked and Q-switched operations can be readily realized using the SnS-SA. Moreover, the better chemical stability of SnS over BP shows its potential in pulse laser generation. It is worthwhile to note the contribution of the long decay time of the dynamic process is less than 10%; thus an optical modulation speed as high as terahertz is promised, e.g., gigahertz mode-locking operations.

D. Ultrafast Photonic Applications of SnS NSs

In general, passive Q switching and mode locking are effective techniques to generate short pulses in bulk lasers. The high-quality SnS-SA facilitates the generation of short and ultrashort pulses by the two techniques. Taking the advantage of the large modulation depth and moderate response time, a passive Q-switching operation is initially generated from the fiber laser. As described previously [73], there is a critical parameter: $E^2 = E_G E_{SA} \Delta T$, where E_{SA} and ΔT represent the saturation energy and modulation depth of the SnS-SA, and E_G is the gain saturation energy of the laser. In the cavity, when the single pulse energy E_p matches the relation of $E_p < E^2$, the Q switching can be obtained. Otherwise, the continuous wave (CW) mode-locked operation may be achieved. It is worth noting that changing the E_{SA} and ΔT with the assistance of adjusting the deposition surface of SnS NSs on microfiber is the convenient way to modify the value of E, as E_G is determined by the gain fiber and is hardly modified.

Q-switched pulses are established when the pump power is increased to 150 mW. However, the pulses cannot be stabilized until the pump power is increased to 275 mW. The pulse repetition rate was 36.36 kHz for 275 mW and increased with the pump power, as Figs. 6(a)–6(e) show. The large scanning range of Q-switched pulse train in Fig. 6(f) indicates the long-term
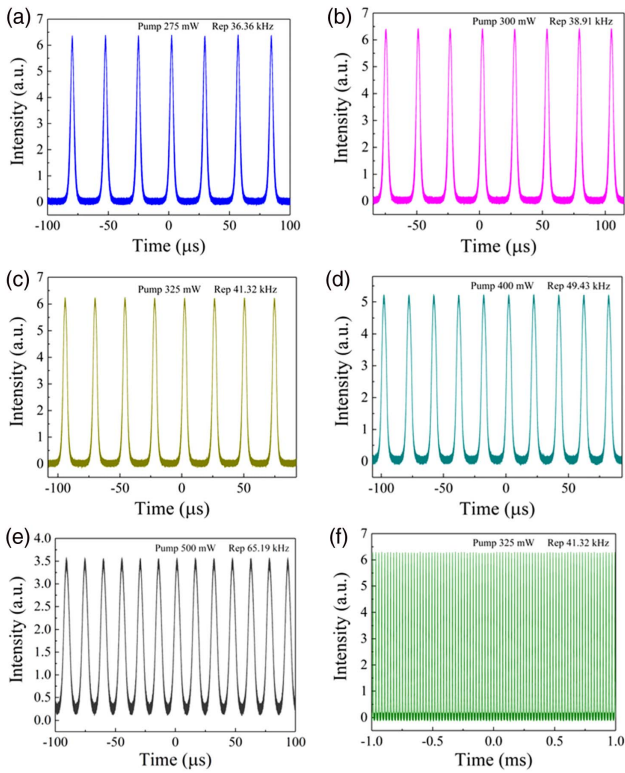
Fig. 6. *Q*-switched pulse trains at different pump powers. (a) 275 mW with repetition rate of 36.36 kHz; (b) 300 mW with repetition rate of 38.91 kHz; (c) 325 mW with repetition rate of 41.32 kHz; (d) 400 mW with repetition rate of 49.43 kHz; (e) 500 mW with repetition rate of 65.19 kHz; (f) long-term stability of the *Q*-switched state.

stability of the *Q*-switched state. Besides, once the pump power exceeded 500 mW, the *Q*-switched state turned to be unstable again, and the *Q*-switched state disappeared. If the pump power exceeded 600 mW, a CW state would be obtained. The evolution of averaged output power and repetition rate as the function of pump power is shown in Fig. 7(a). Both of them increased almost linearly versus the pump power up to 375 mW. The radio-frequency (RF) spectrum of the established *Q*-switched pulses at a pump power of 325 mW, giving a high signal-to-noise ratio up to ∼50 dB, indicated the extremely stable *Q*-switching state.

Passive CW mode locking is a convenient and effective way to generate ultrashort pulses, demanding the appropriate
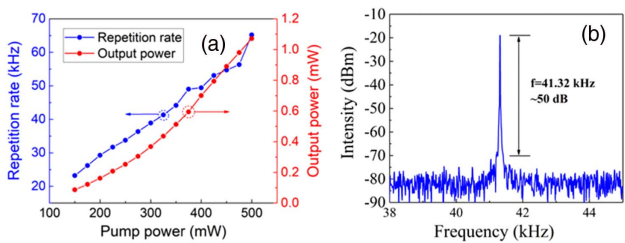

Fig. 7. (a) Evolution of averaged output power and pulse repetition rate as the pump power increases; (b) RF spectrum under the pump power of 325 mW.
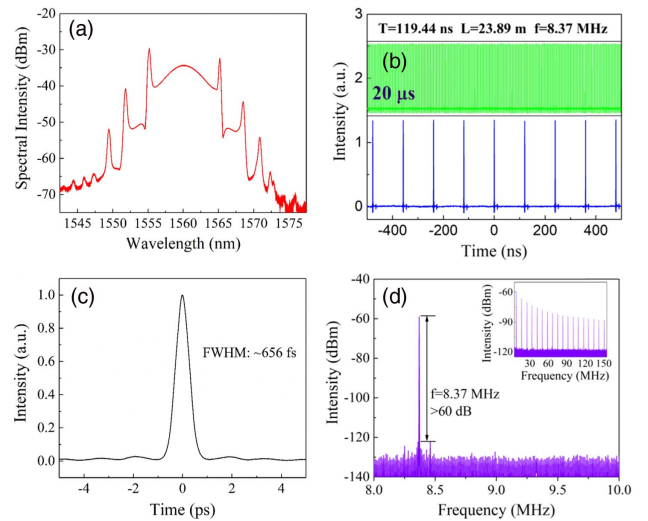

Fig. 8. Mode-locked performance. (a) Optical spectrum; (b) pulse train; (c) autocorrelation trace; (d) RF spectrum.

modulation depth, saturation recovery time, and fine cavity design. Ultrashort and high repetition-rate mode-locked pulses are self-started after carefully adjusting the pump power and optimizing the cavity design. A typical mode-locked state is shown in Fig. 8. The generated pulses are recorded by a 1 GHz-high-speed oscilloscope, showing the fundamental repetition rate of 8.37 MHz, which matches well with the cavity length. A large scanning range of pulse trains at a scale bar of 20 μs shows no fluctuation, proving the stable operation of the mode-locked fiber laser. The mode-locked spectrum of the pulses is centered at ∼1560 nm and the full width at half-maximum (FWHM) bandwidth is ∼5.28 nm. Clear and distinct Kelly sidebands in the spectrum [Fig. 8(a)], a typical characteristic of the soliton fiber lasers with net anomalous dispersion, indicate that the mode-locked pulses can be shaped into optical soliton pulses. The pulse width was measured to be 656 fs by an intensity autocorrelator, assuming the sech^2 intensity profile [see Fig. 8(c)]. The calculated time-bandwidth product is ∼0.384, indicating a slight pulse chirp.

The mode-locked laser operates at a highly stable state, for the measured signal-to-noise ratio more than 60 dB from the RF spectrum. To further reveal the long-term stability of mode locking, the mode-locked spectrum at the pump power of 135 mW is recorded over 6 h. No obvious
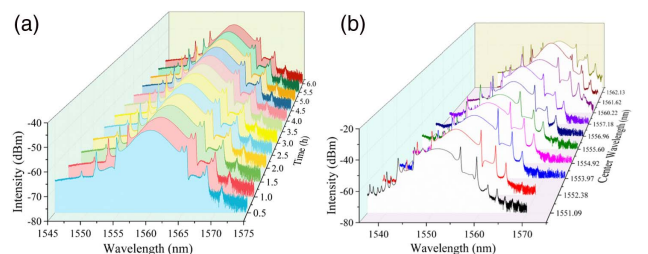

Fig. 9. (a) Long-term operation of SnS NSs-based mode locking and (b) its tunable wavelength.

optical spectrum drift was observed [Fig. 9(a)], proving the stable operation.

3. CONCLUSIONS

SnS, as a rising two-elemental and 2D BP-analog group IV monochalcogenide, removes the main obstacle of BP in long-term stability. High-performance 2D SnS was successfully obtained using the LPE method, and its high stability for 1 month has been confirmed by standard and comprehensive characterization techniques. The excellent saturable absorption properties of SnS were found with large and tunable optical modulation depth (maximum value of 36.4%). The saturation optical intensity ($\sim$34.8 GW/cm^2) is 1 order smaller than that of the BP ($\sim$334.6 GW/cm^2), which significantly reduces the threshold of the SA-based pulse lasers. The response time was characterized to be $\tau_1 = 873$ fs and $\tau_2 = 96.9$ ps with the assistance of femtosecond-resolved TA spectra, indicating SnS can be used as a high-speed modulator in the range of gigahertz and even terahertz. Using the SnS as an efficient SA, passive Q switching and CW mode locking were successfully demonstrated in an identical resonator with high stability. An ultrashort laser pulse sustained for 656 fs was readily obtained. Our systematic study shows that the two-elemental BP-analog SnS is definitely a new type of promising SA, with high stability and robust optical performance compared to single-elemental BP. This could compensate for the main drawbacks of BP and boost the ultrafast photonics of BP-analog materials, such as the group IV monochalcogenides.

†These authors contributed equally to this work.

REFERENCES

1. F. Xia, H. Wang, and Y. Jia, "Rediscovering black phosphorus as an anisotropic layered material for optoelectronics and electronics," Nat. Commun. **5**, 4458 (2014).
2. S. Lin, S. Liu, Z. Yang, Y. Li, T. W. Ng, Z. Xu, Q. Bao, J. Hao, C. Lee, and C. Surya, "Solution-processable ultrathin black phosphorus as an effective electron transport layer in organic photovoltaics," Adv. Funct. Mater. **26**, 864–871 (2016).
3. Y. Wang, G. Huang, H. Mu, S. Lin, J. Chen, S. Xiao, Q. Bao, and J. He, "Ultrafast recovery time and broadband saturable absorption properties of black phosphorus suspension," Appl. Phys. Lett. **107**, 091905 (2015).
4. V. Tran, R. Soklaski, Y. Liang, and L. Yang, "Layer-controlled band gap and anisotropic excitons in few-layer black phosphorus," Phys. Rev. B **89**, 235319 (2014).
5. S. B. Lu, L. L. Miao, Z. N. Guo, X. Qi, C. J. Zhao, H. Zhang, S. C. Wen, D. Y. Tang, and D. Y. Fan, "Broadband nonlinear optical response in multi-layer black phosphorus: an emerging infrared and mid-infrared optical material," Opt. Express **23**, 11183–11194 (2015).
6. D. Li, A. E. D. R. Castillo, H. Jussila, G. Ye, Z. Ren, J. Bai, X. Chen, H. Lipsanen, Z. Sun, and F. Bonaccorso, "Black phosphorus polycarbonate polymer composite for pulsed fibre lasers," Appl. Mater. Today **4**, 17–23 (2016).
7. C. Zhao, D. Fan, D. Tang, G. Jiang, H. Zhang, Q. Bao, S. Wen, S. Chen, X. Yu, and Y. Chen, "Mechanically exfoliated black phosphorus as a new saturable absorber for both Q-switching and mode-locking laser operation," Opt. Express **23**, 12823–12833 (2015).
8. H. Mu, S. Lin, Z. Wang, S. Xiao, P. Li, Y. Chen, H. Zhang, H. Bao, P. L. Shu, and C. Pan, "Pulsed lasers: black phosphorus–polymer composites for pulsed lasers," Adv. Opt. Mater. **3**, 1447–1453 (2015).
9. J. O. Island, G. A. Steele, H. S. J. van der Zant, and A. Castellanos-Gomez, "Environmental instability of few-layer black phosphorus," 2D Mater. **2**, 11002 (2014).
10. A. Castellanosgomez, L. Vicarelli, E. Prada, J. O. Island, K. L. Narasimhaacharya, S. I. Blanter, D. J. Groenendijk, M. Buscema, G. A. Steele, and J. V. Alvarez, "Isolation and characterization of few-layer black phosphorus," 2D Mater. **1**, 25001 (2014).
11. R. A. Doganov, E. C. O'Farrell, S. P. Koenig, Y. Yeo, A. Ziletti, A. Carvalho, D. K. Campbell, D. F. Coker, K. Watanabe, and T. Taniguchi, "Transport properties of pristine few-layer black phosphorus by van der Waals passivation in an inert atmosphere," Nat. Commun. **6**, 6647 (2015).
12. M. Buscema, D. J. Groenendijk, S. I. Blanter, G. A. Steele, H. S. J. van der Zant, and A. Castellanosgomez, "Fast and broadband photoresponse of few-layer black phosphorus field-effect transistors," Nano Lett. **14**, 3347–3352 (2014).
13. A. Favron, E. Gaufrès, F. Fossard, A. L. Phaneuf-L'Heureux, Y. W. Tang, P. L. Lévesque, A. Loiseau, R. Leonelli, S. Francoeur, and R. Martel, "Photooxidation and quantum confinement effects in exfoliated black phosphorus," Nat. Mater. **14**, 826–832 (2015).
14. A. Avsar, I. J. Veramarun, J. Y. Tan, K. Watanabe, T. Taniguchi, A. H. C. Neto, and B. Özyilmaz, "Air-stable transport in graphene-contacted, fully encapsulated ultrathin black phosphorus-based field-effect transistors," ACS Nano **9**, 4138–4145 (2015).
15. J. D. Wood, S. A. Wells, D. Jariwala, K. S. Chen, E. Cho, V. K. Sangwan, X. Liu, L. J. Lauhon, T. J. Marks, and M. C. Hersam, "Effective passivation of exfoliated black phosphorus transistors against ambient degradation," Nano Lett. **14**, 6964–6970 (2014).
16. C. R. Ryder, J. D. Wood, S. A. Wells, Y. Yang, D. Jariwala, T. J. Marks, G. C. Schatz, and M. C. Hersam, "Covalent functionalization and passivation of exfoliated black phosphorus via aryl diazonium chemistry," Nat. Chem. **8**, 597–602 (2016).
17. Y. Zhao, H. Wang, H. Huang, Q. Xiao, Y. Xu, Z. Guo, H. Xie, J. Shao, Z. Sun, and W. Han, "Surface coordination of black phosphorus for robust air and water stability," Angew. Chemie **55**, 5003–5007 (2016).
18. T. Xian, W. Liang, J. Zhao, Z. Li, Q. Meng, T. Fan, C. S. Luo, Z. Ye, L. Yu, and Z. Guo, "Fluorinated phosphorene: electrochemical synthesis, atomistic fluorination, and enhanced stability," Small **13**, 1702739 (2017).
19. S. Tan, I. Abdelwahab, L. Chu, S. M. Poh, Y. Liu, J. Lu, W. Chen, and K. P. Loh, "Quasi-monolayer black phosphorus with high mobility and air stability," Adv. Mater. **30**, 1704619 (2018).
20. Z. Guo, S. Chen, Z. Wang, Z. Yang, F. Liu, Y. Xu, J. Wang, Y. Yi, H. Zhang, and L. Liao, "Metal-ion-modified black phosphorus with enhanced stability and transistor performance," Adv. Mater. **29**, 1703811 (2017).
21. X. Chen, Y. Wu, Z. Wu, Y. Han, S. Xu, L. Wang, W. Ye, T. Han, Y. He, and Y. Cai, "High-quality sandwiched black phosphorus heterostructure and its quantum oscillations," Nat. Commun. **6**, 7315 (2014).
22. C. Xing, G. Jing, X. Liang, M. Qiu, Z. Li, R. Cao, X. Li, D. Fan, and H. Zhang, "Graphene oxide/black phosphorus nanoflake aerogels with robust thermo-stability and significantly enhanced photothermal properties in air," Nanoscale **9**, 8096–8101 (2017).
23. J. Na, Y. T. Lee, J. A. Lim, D. K. Hwang, G. T. Kim, W. K. Choi, and Y. W. Song, "Few-layer black phosphorus field-effect transistors with reduced current fluctuation," ACS Nano **8**, 11753–11762 (2014).

24. Y. Zhao, Q. Zhou, Q. Li, X. Yao, and J. Wang, "Passivation of black phosphorus via self-assembled organic monolayers by van der Waals epitaxy," Adv. Mater. **29**, 1603990 (2017).

25. M. Qiu, D. Wang, W. Liang, L. Liu, Y. Zhang, X. Chen, D. K. Sang, C. Xing, Z. Li, and B. Dong, "Novel concept of the smart NIR-light-controlled drug release of black phosphorus nanostructure for cancer therapy," Proc. Natl. Acad. Sci. **115**, 501–506 (2018).

26. L. Li, Z. Chen, Y. Hu, X. Wang, T. Zhang, W. Chen, and Q. Wang, "Single-layer single-crystalline SnSe nanosheets," J. Am. Chem. Soc. **135**, 1213–1216 (2013).

27. D. Xue, J. Tan, J. Hu, W. Hu, Y. Guo, and L. Wan, "Anisotropic photoresponse properties of single micrometer-sized GeSe nanosheet," Adv. Mater. **24**, 4528–4533 (2012).

28. S. Zhang, N. Wang, S. Liu, S. Huang, W. Zhou, B. Cai, M. Xie, Q. Yang, X. Chen, and H. Zeng, "Two-dimensional GeS with tunable electronic properties via external electric field and strain," Nanotechnology **27**, 274001 (2016).

29. C. Xin, J. Zheng, Y. Su, S. Li, B. Zhang, Y. Feng, and F. Pan, "Few-layer tin sulfide: a new black-phosphorus-analogue 2D material with a sizeable band gap, odd–even quantum confinement effect, and high carrier mobility," J. Phys. Chem. C **120**, 22663–22669 (2016).

30. L. D. Zhao, S. H. Lo, Y. Zhang, H. Sun, G. Tan, C. Uher, C. Wolverton, V. P. Dravid, and M. G. Kanatzidis, "Ultralow thermal conductivity and high thermoelectric figure of merit in SnSe crystals," Nature **508**, 373–377 (2014).

31. L. D. Zhao, G. Tan, S. Hao, J. He, Y. Pei, H. Chi, H. Wang, S. Gong, H. Xu, and V. P. Dravid, "Ultrahigh power factor and thermoelectric performance in hole-doped single-crystal SnSe," Science **351**, 141–144 (2015).

32. A. Rodin, L. Gomes, A. Carvalho, and A. Castro Neto, "Valley physics in tin (II) sulfide," Phys. Rev. B **93**, 045431 (2016).

33. M. Wu and X. C. Zeng, "Intrinsic ferroelasticity and/or multiferroicity in two-dimensional phosphorene and phosphorene analogues," Nano Lett. **16**, 3236–3241 (2016).

34. R. Fei, W. Kang, and L. Yang, "Ferroelectricity and phase transitions in monolayer group-IV monochalcogenides," Phys. Rev. Lett. **117**, 097601 (2016).

35. M. Mehboudi, A. M. Dorio, W. Zhu, Zande, A. van der Zande, H. O. H. Churchill, A. A. Pachecosanjuan, E. O. Harriss, P. Kumar, and S. Barrazalopez, "Two-dimensional disorder in black phosphorus and monochalcogenide monolayers," Nano Lett. **16**, 1704–1712 (2015).

36. C. Chang, M. Wu, D. He, Y. Pei, C. Wu, X. Wu, H. Yu, F. Zhu, K. Wang, Y. Chen, and L. Huang, "3D charge and 2D phonon transports leading to high out-of-plane ZT in N-type SnSe crystals," Science **360**, 778–783 (2018).

37. Z. Tian, C. Guo, M. Zhao, R. Li, and J. Xue, "Two-dimensional SnS: a phosphorene analogue with strong in-plane electronic anisotropy," ACS Nano **11**, 2219–2226 (2016).

38. R. Fei, W. Li, J. Li, and L. Yang, "Giant piezoelectricity of monolayer group IV monochalcogenides," Appl. Phys. Lett. **107**, 173104 (2015).

39. J. Xia, X. Z. Li, X. Huang, N. Mao, D. D. Zhu, L. Wang, H. Xu, and X. M. Meng, "Physical vapor deposition synthesis of two-dimensional ortho-rhombic SnS flakes with strong angle/temperature-dependent Raman responses," Nanoscale **8**, 2063–2070 (2015).

40. S. M. Herron, J. T. Tanskanen, K. E. Roelofs, and S. F. Bent, "Highly textured tin(II) sulfide thin films formed from sheetlike nanocrystal inks," Chem. Mater. **26**, 7106–7113 (2014).

41. R. E. Banai, L. A. Burton, S. G. Choi, F. Hoferrr, T. Sorgenfrei, A. Walsh, B. To, A. Cröll, and J. R. S. Brownson, "Ellipsometric characterization and density-functional theory analysis of anisotropic optical properties of single-crystal α-SnS," J. Appl. Phys. **116**, 013511 (2014).

42. N. K. Reddy, M. Devika, and E. S. R. Gopal, "Review on tin (II) sulfide (SnS) material: synthesis, properties, and applications," Crit. Rev. Solid State Mater. Sci. **40**, 1–37 (2015).

43. L. Peng, C. Wang, Q. Qian, C. Bi, S. Wang, and Y. Huang, "Complete separation of carriers in the GeS/SnS lateral heterostructure by uniaxial tensile strain," ACS Appl. Mater. Interfaces **9**, 40969–40977 (2017).

44. J. Xia, D. Zhu, X. Li, L. Wang, L. Tian, J. Li, J. Wang, X. Huang, and X. Meng, "Epitaxy of layered orthorhombic SnS–SnS$_x$Se$_{(1-x)}$ core–shell

heterostructures with anisotropic photoresponse," Adv. Funct. Mater. **26**, 4673–4679 (2016).

45. H. Zhu, D. Yang, Y. Ji, Z. Hui, and X. Shen, "Two-dimensional SnS nanosheets fabricated by a novel hydrothermal method," J. Mater. Sci. **40**, 591–595 (2005).

46. M. Sharon and K. Basavaswaran, "Photoelectrochemical behaviour of tin monosulphide," Sol. Cells **25**, 97–107 (1988).

47. Z. Xie, D. Wang, T. Fan, C. Xing, Z. Li, W. Tao, L. Liu, D. Fan, and H. Zhang, "Black phosphorus analogue tin sulfide nanosheets: synthesis and application as near-infrared photothermal agents and drug delivery platforms for cancer therapy," J. Mater. Chem. B **6**, 4747–4755 (2018).

48. V. Steinmann, R. Jaramillo, K. Hartman, R. Chakraborty, R. E. Brandt, J. R. Poindexter, Y. S. Lee, L. Sun, A. Polizzotti, and H. H. Park, "3.88% efficient tin sulfide solar cells using congruent thermal evaporation," Adv. Mater. **26**, 7488–7492 (2014).

49. P. Sinsermsuksakul, L. Sun, S. W. Lee, H. H. Park, S. B. Kim, C. Yang, and R. G. Gordon, "Overcoming efficiency limitations of SnS-based solar cells," Adv. Energy Mater. **4**, 1400496 (2015).

50. T. Zhou, W. K. Pang, C. Zhang, J. Yang, Z. Chen, H. K. Liu, and Z. Guo, "Enhanced sodium-ion battery performance by structural phase transition from two-dimensional hexagonal-SnS$_2$ to orthorhombic-SnS," ACS Nano **8**, 8323–8333 (2014).

51. S. Hwang, Z. Yao, L. Zhang, M. Fu, K. He, L. Mai, C. Wolverton, and D. Su, "Multistep lithiation of tin sulfide: an investigation using *in situ* electron microscopy," ACS Nano **12**, 3638–3645 (2018).

52. H. Wu, X. Lu, G. Wang, K. Peng, H. Chi, B. Zhang, Y. Chen, C. Li, Y. Yan, L. Guo, and C. Uher, "Sodium-doped tin sulfide single crystal: a nontoxic earth-abundant material with high thermoelectric performance," Adv. Energy Mater. **8**, 1800087 (2018).

53. K. Szendrei-Temesi, O. Sanchez-Sobrado, S. B. Betzler, K. M. Durner, T. Holzmann, and B. V. Lotsch, "Lithium tin sulfide—a high-refractive-index 2D material for humidity-responsive photonic crystals," Adv. Funct. Mater. **28**, 1705740 (2018).

54. H. Wang, D. Chao, J. Liu, J. Lin, and Z. Shen, "Nanoengineering of 2D tin sulfide nanoflake arrays incorporated on polyaniline nanofibers with boosted capacitive behavior," 2D Mater. **5**, 031005 (2018).

55. W. Cheng, N. Singh, W. Elliott, J. Lee, A. Rassoolkhani, X. Jin, E. W. Mcfarland, and S. Mubeen, "Earth-abundant tin sulfide-based photocathodes for solar hydrogen production," Adv. Sci. **5**, 1700362 (2018).

56. J. R. Brent, D. J. Lewis, T. Lorenz, E. A. Lewis, N. Savjani, S. J. Haigh, G. Seifert, B. Derby, and P. O'Brien, "Tin(II) sulfide (SnS) nanosheets by liquid-phase exfoliation of herzenbergite: IV-VI main group two-dimensional atomic crystals," J. Am. Chem. Soc. **137**, 12689–12696 (2015).

57. A. M. Tripathi and S. Mitra, "Tin sulfide (SnS) nanorods: structural, optical and lithium storage property study," RSC Adv. **4**, 10358–10366 (2014).

58. J. Chao, Z. Wang, X. Xu, Q. Xiang, W. Song, G. Chen, J. Hu, and D. Chen, "Tin sulfide nanoribbons as high performance photoelectrochemical cells, flexible photodetectors and visible-light-driven photocatalysts," RSC Adv. **3**, 2746–2753 (2012).

59. X. Jiang, S. Liu, W. Liang, S. Luo, Z. He, Y. Ge, H. Wang, R. Cao, F. Zhang, and Q. Wen, "Broadband nonlinear photonics in few-layer MXene Ti$_3$C$_2$T$_x$ (T = F, O, or OH)," Laser Photon. Rev. **12**, 1700229 (2018).

60. K. Wang, Y. Ju, J. He, L. Zhang, Y. Chen, W. J. Blau, and J. Wang, "Nonlinear optical propagation in a tandem structure comprising nonlinear absorption and scattering materials," Appl. Phys. Lett. **104**, 021110 (2014).

61. C. B. de Araújo, A. S. Gomes, and G. Boudebs, "Techniques for nonlinear optical characterization of materials: a review," Rep. Prog. Phys. Phys. Soc. **79**, 036401 (2016).

62. E. Sani and A. Dell'Oro, "Spectral optical constants of ethanol and isopropanol from ultraviolet to far infrared," Opt. Mater. (Amsterdam) **60**, 137–141 (2016).

63. C. Zhu, F. Wang, Y. Meng, X. Yuan, F. Xiu, H. Luo, Y. Wang, J. Li, X. Lv, and L. He, "A robust and tuneable mid-infrared optical switch enabled by bulk Dirac fermions," Nat. Commun. **8**, 14111 (2017).

64. L. Lu, Z. Liang, L. Wu, Y. X. Chen, Y. Song, S. C. Dhanabalan, J. S. Ponraj, B. Dong, Y. Xiang, and F. Xing, "Few-layer bismuthene: sonochemical exfoliation, nonlinear optics and applications for

ultrafast photonics with enhanced stability," Laser Photon. Rev. **12**, 1700221 (2018).

65. Y. Song, Z. Liang, X. Jiang, Y. Chen, Z. Li, L. Lu, Y. Ge, K. Wang, J. Zheng, and S. Lu, "Few-layer antimonene decorated microfiber: ultrashort pulse generation and all-optical thresholding with enhanced long term stability," 2D Mater. **4**, 045010 (2017).

66. C. Xing, Z. Xie, Z. Liang, W. Liang, T. Fan, J. S. Ponraj, S. C. Dhanabalan, D. Fan, and H. Zhang, "Selenium nanosets: 2D nonlayered selenium nanosheets: facile synthesis, photoluminescence, and ultrafast photonics," Adv. Opt. Mater. **5**, 1700884 (2017).

67. C. Ruckebusch, M. Sliwa, P. Pernot, Juan, A. De, and R. Tauler, "Comprehensive data analysis of femtosecond transient absorption spectra: a review," J. Photochem. Photobiol. C Photochem. Rev. **13**, 1–27 (2012).

68. U. Keller, "Recent developments in compact ultrafast lasers," Nature **424**, 831–838 (2003).

69. Q. Bao, Z. Han, W. Yu, Z. Ni, Y. Yan, Z. X. Shen, K. P. Loh, and Y. T. Ding, "Atomic-layer graphene as a saturable absorber for ultrafast pulsed lasers," Adv. Funct. Mater. **19**, 3077–3083 (2010).

70. J. Ma, H. Huang, K. Ning, X. Xu, G. Xie, L. Qian, K. P. Loh, and D. Tang, "Generation of 30 fs pulses from a diode-pumped graphene mode-locked Yb:CaYAlO$_4$ laser," Opt. Lett. **41**, 890–893 (2016).

71. S. Wang, H. Yu, H. Zhang, A. Wang, M. Zhao, Y. Chen, L. Mei, and J. Wang, "Broadband few-layer MoS$_2$ saturable absorbers," Adv. Mater. **26**, 3538–3544 (2014).

72. R. Paschotta and U. Keller, "Passive mode locking with slow saturable absorbers," Appl. Phys. B **73**, 653–662 (2001).

73. Y. Chen, G. Jiang, S. Chen, Z. Guo, X. Yu, C. Zhao, H. Zhang, Q. Bao, S. Wen, and D. Tang, "Mechanically exfoliated black phosphorus as a new saturable absorber for both *Q*-switching and mode-locking laser operation," Opt. Express **23**, 12823–12833 (2015).